EPJ E
Soft Matter and
Biological Physics

EPJ.org
your physics journal

Eur. Phys. J. E (2011) **34**: 58 DOI: 10.1140/epje/i2011-11058-y

Time-resolved microfocused small angle X-ray scattering investigation of the microfluidic concentration of charged nanoparticles

A. Merlin, J. Angly, L. Daubersies, C. Madeira, S. Schoeder, J. Leng and J.-B. Salmon

EDP SCIENCES
Società Italiana di Fisica
Springer

Eur. Phys. J. E (2011) **34**: 58
DOI 10.1140/epje/i2011-11058-y

THE EUROPEAN PHYSICAL JOURNAL E

Regular Article

Time-resolved microfocused small-angle X-ray scattering investigation of the microfluidic concentration of charged nanoparticles[⋆]

A. Merlin[1], J. Angly[1], L. Daubersies[1], C. Madeira[1], S. Schöder[2], J. Leng[1], and J.-B. Salmon[1,a]

[1] LOF, UMR 5258 Rhodia-CNRS-Bordeaux 1, 178 avenue du Docteur Schweitzer, F–33608 Pessac cedex, France
[2] European Synchrotron Radiation Facility, 6 rue Jules Horowitz, BP 220, 38043 Grenoble, France

Received 30 March 2011

Abstract. We describe the concentration process of a dispersion of silica nanoparticles undergoing evaporation in a dedicated microfluidic device. Using microfocused small-angle X-ray scattering, we measure in time and space both the concentration field of the dispersion and its structure factor. We show that the electrostatic interactions affect the concentration rate by strongly enhancing the collective diffusion coefficient of the nanoparticle dispersion. *En route* towards high concentrations, the nanoparticles eventually undergo a liquid-solid phase transition in which we evidence crystallites of micron size.

1 Introduction

The spontaneous or guided self-assembly of functional nanoparticles (NPs) into three-dimensional ordered structures has recently driven a flourishing interest due to the possible *bottom-up* fabrication of materials with unprecedented properties at the 10–100 nm scale, such as metamaterials and plasmonic nanostructures [1–3]. In most cases, self-assembly occurs during the evaporation of a sessile droplet of an organic NP dispersion left on a substrate, typically a microscopy grid, and results mainly in two-dimensional structures, thereby emphasizing the crucial role of particle-interface interactions [4]. Beside, only few studies show real-time, *in situ* monitoring of the formation of such ordered structures in evaporating droplets [5,6]. These investigations are indeed difficult to perform not only because both the NP concentration and local ordering need to be characterized both in space and time with a fine resolution but also because the kinetics of drying is itself complex to model [7,8], making the fundamental information even harder to extract.

In the present work, we use *microfluidic evaporation* [9] to bring a fine good control both on the geometry and on evaporation, and couple it to *microfocused* small-angle X-ray scattering (SAXS). The combination of the two techniques allows us to overcome most the above-mentioned difficulties and leads to a time- and space-resolved quantitative information about the NP concentration process, up to the occurrence of 3D ordered structures.

Microevaporation has been described recently [9–11] as a means to control at microscale the process of concentrating a solution. It exploits the pervaporation of water through a thin polymeric membrane (fig. 1) in order to extract the solvent only and to locally increase the concentration; close to the tip of a microevaporator, a gradient of concentration builds up and develops in a *controlled manner*. This technique is analogous to classical sedimentation/centrifugation experiments, but permits to concentrate any solution or dispersion —including molecules and NPs up to a solid state thanks to the microfluidic benefits— or to ultrafiltration experiments, yet with a greatly facilitated observation. *In fine*, it permits to extract thermodynamic and dynamic properties of mixtures [12].

Using *in situ* microfocused SAXS experiments performed directly on the polymeric microevaporation device, we monitored the concentration process of an aqueous dispersion of charged silica NPs (radius $R = 13\,\mathrm{nm}$), and measured both their concentration ϕ and their structure, in space and time with a μm spatial resolution. Owing to a thorough (and tedious yet standard) signal processing, our experiments unveil important aspects of the concentration process. First, below $\phi < 30\%$ (volume fraction), our experiments reveal that electrostatic interactions strongly enhance the collective diffusion coefficient of the NPs dispersion, which directly influences NPs concentration gradients upon concentration. Then, we observe that NPs

---

[⋆] Supplementary material in the form of two .mpg files available from the Journal web page at
`http://dx.doi.org/10.1140/epje/i2011-11058-y`

[a] e-mail: `jean-baptiste.salmon-exterieur@eu.rhodia.com`

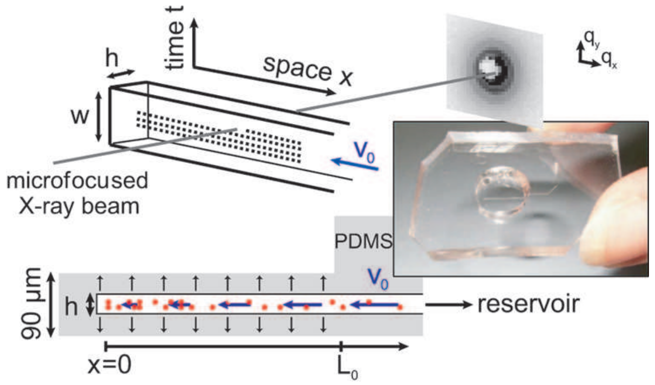

Fig. 1. Bottom: cross-section view of our microevaporator and picture of the real device. The microchannel (width×height $w \times h = 350 \times 52\,\mu\text{m}^2$) is connected to a reservoir containing the NPs dispersion. Pervaporation occurs through the thin PDMS walls on the length $L_0 = 6.2$ mm. Top: sketch of the microfocused SAXS experiments. The X-ray beam is focused on the main channel (focal spot $1.5 \times 1.5\,\mu\text{m}^2$), and 2D patterns are collected on a CCD camera at $= 492$ mm from the sample. Space-time acquisition is performed on a x-grid with $50\,\mu$m steps (81 points on 4 mm), on different lines displaced in the y-direction by $0.5\,\mu$m to avoid beam damage. The temporal resolution is ≈ 160 s between each consecutive measurement at a given x-position.

concentrate up to the growth of a *solid* state at a volume fraction $\phi \approx 30\%$ marked by strong spatial correlations. Finally, the microfocused SAXS resolution allows us to identify unambiguously long-range–ordered, 3D structures with a typical grain size of several micrometers within the solid phase.

2 Setup and experiments

2.1 System investigated

We investigate the microevaporation of an aqueous dispersion of negatively charged silica NPs, Ludox AS40 (radius 13 nm). Ludox silica NPs are often used as a model system, and one can thus easily find in the literature characterizations of such NPs (see, for instance, ref. [13]). The original stock dispersion (measured concentration of $42 \pm 0.2\%$ by weight) was diluted with deionised water (Milli-Q) to reach a dispersion at a volume fraction of $\phi_0 = 1.4\%$ (we assume the density of silica NPs to be 2.2 g/mL). The stock dispersion also contains small amounts of ionic species, Na_2SO_4 and NaCl at 0.005 and 0.007% wt., respectively (data of the manufacturer) so that the final dilute dispersion displays a total concentration of ionic species of about 0.2 mM, and its measured pH is 7.5 at 22 °C. According to several measurements found in the literature [13,14], the effective charge carried by the Ludox NPs is in the 50–70 range in the relevant investigated pH.

2.2 Microevaporator fabrication

Performing small-angle X-ray scattering measurements using synchrotron radiation directly on a polydimethylsiloxane (PDMS) microfluidic chip is often a real challenge (beam damage, X-ray absorption and scattering, ...). Therefore, specific materials are often used to manufacture microfluidic devices suitable for X-ray analysis (polyimide films [15,16], silicon nitride windows [17]). Here, we exploit the thinness of the PDMS membranes of the microevaporator to perform SAXS analysis despite the difficulties mentioned above. Figure 1 sketches our setup and the experiment. We have manufactured a microevaporator specific for X-ray compatibility using standard soft lithography. The main channel is embedded in a thin PDMS membrane (total thickness $\approx 90\,\mu$m), and stuck on a thicker PDMS stamp for mechanical stability (photo in fig. 1). The main channel is connected to a tube, the reservoir, containing the dilute aqueous dispersion of silical NPs. Pervaporation occurs through the side-wall membranes, and induces a net stationary flow at velocity v_0 that drives and concentrates the charged NPs up to the tip of the microevaporator. The corresponding flux $\phi_0 v_0$ depends on the incoming velocity v_0 which has been calibrated in a preliminary step. For this, we filled the device with deionized water and dried up the reservoir; the resulting air/water meniscus moves towards the tip of the microevaporator because of pervaporation and we monitored its velocity and found $v_0 = 5.5 \pm 0.5\,\mu$m/s. We also checked using local velocimetry measurements done on fluorescent tracers that this velocity is indeed that of the flow even in the absence of meniscus.

2.3 Microfocused SAXS experiments

We place the microfluidic device on a fully automated x-y-z positioning platform located at the focal point of a high-brilliance, microfocused X-ray beamline [18,19]. The incoming beam is tightly focused (spot size $\approx 1.5\,\mu$m) on the PDMS chip, and 2D SAXS patterns are collected using a CCD detector covering a q-range of 0.24 to $6\,\text{nm}^{-1}$. The exposure time is optimized at 1 s in order to maximize the signal while minimizing the beam damage; the latter was carefully evaluated using *in situ* SAXS, and *post mortem* scanning electron microscopy and Raman confocal spectroscopy (data not shown), ensuring that our thin PDMS membranes were neither punched nor significantly chemically altered by such an intense beam.

To monitor in space and time the NP concentration profiles in the chip, the latter is moved horizontally perpendicular to the beam after every measurement (along x-lines, see fig. 1). Then, to further reduce the beam damage, the sample is slightly displaced vertically after one line is completed (y-direction, see fig. 1). We subtract from the measurements the reference pattern collected on a twin microchannel containing pure water only, and also correct for the decay of the primary beam intensity.

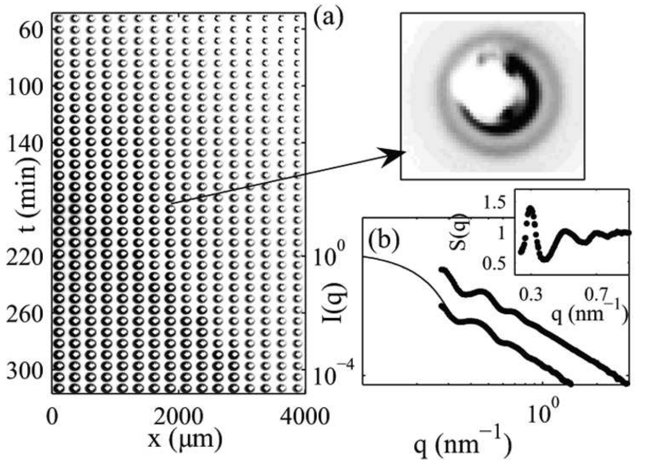

Fig. 2. (a) Spatio-temporal composite image of the 2D SAXS patterns. (b) Azimuthal average $I(q)$ for the first measured spectra (at $x = 4\,\text{mm}$ and $t = 49\,\text{min}$ due to experimental constraints of filling and aligning the device): the continuous line represents the form factor of polydisperse spheres (best fit with $R = (13 \pm 1.7)\,\text{nm}$); the upper spectrum corresponds to a typical $I(q)$ ($t = 290\,\text{min}$, $x = 350\,\mu\text{m}$) from which both the concentration $\phi(x,t)$ and the structure factor $S(q)$ (insert) are extracted.

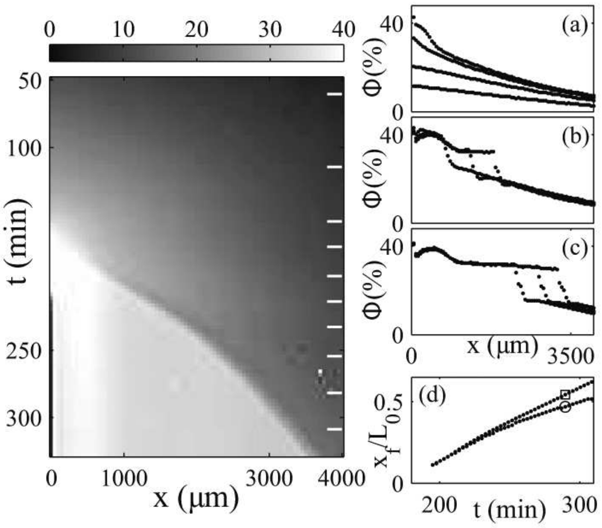

Fig. 3. Left: spatio-temporal plot of the concentration ϕ. (a)–(c) show some concentration profiles at the times indicated by white ticks on the spatio-temporal plot. (d) Position of the front x_f against time, measured (○) or calculated from the solute conservation (□).

3 Results: overview of the concentration process

3.1 SAXS analysis

Figure 2(a) shows a composite image of the 2D SAXS patterns that summarizes the spatio-temporal concentration process of the charged NPs. Such a composite image gathers the SAXS patterns (2D arrays q_x-q_y) collected by the detector at times t, and at each x-position in the microchannel (for a reason of size, fig. 2(a) does not display the ≈ 9000 SAXS images collected). We then perform an azimuthal averaging of these data to get the scattering curves $I(q)$ at each x-t point (fig. 2(b)).

The first measured curve ($x = 4\,\text{mm}$, $t = 49\,\text{min}$) fits well with the form factor of polydisperse spheres $P(q)$, with radius $R = 13\,\text{nm}$ and a Schultz distribution of width $1.7\,\text{nm}$ [20]; the corresponding volume fraction ϕ_i is unknown for now, but is low enough such that $S(q) \approx 1$ for the q-range investigated in the experiments.

At longer time scales and thus at higher concentrations ϕ, we model the curves according to $I(q) \,\alpha\, \phi S(q) P(q)$, where $S(q)$ is the structure factor of the NP dispersion. Thanks to the constraint $S(q) \to 1$ at large q and the reasonable assumption that the height h of the microchannel remains constant, we can thus estimate both $S(q) = I(q)/(\phi P(q))$ and the relative concentrations ϕ/ϕ_i. At some higher concentrations, structure factors display deep oscillations (inset of fig. 2(b)), thus indicating local ordering of the NPs. Unfortunatly our limited q-range does not allow us to access to the first order of $S(q)$ of the NPs suspension, namely at low concentrations, and it is thus difficult to extract information about the local concentration from the $S(q)$ measurements. *Absolute scale* X-ray measurements would also permit to determine the exact concentration field $\phi(x,t)$ [20], but we cannot measure simultaneously the transmission using the SAXS setup we used. Instead, we can estimate the absolute concentration field $\phi(x,t)$, by using the conservation of mass that stipulates that all the solute that enters the evaporation zone remains trapped in it, *i.e.* $\partial_t \int_0^{L_0} \mathrm{d}x\phi = \phi_0 v_0$. Such measurements have however fairly large uncertainties ($\leq 10\%$) mainly coming from uncertainties on the preliminary v_0 measurements.

3.2 Concentration process: volume fraction measurements

Figure 3 displays the spatio-temporal concentration $\phi(x,t)$ during the evaporation process (see also Movie F1 in the supporting information). Several concentration profiles at different times t indicated by white ticks on this diagram, are also displayed in fig. 3(a)–(c). At small time scales ($t < 170\,\text{min}$), NPs slowly concentrate at the tip of the microevaporator and concentration profiles show only smooth spatial gradients (fig. 3(a)). At $t \approx 170\,\text{min}$, the concentration reaches a maximal value at $x = 0$ of $\phi \approx 40\%$, and a *front* separating a dilute phase from a denser one, starts propagating in the microevaporator as pervaporation still leads to an incoming flux of NPs. Figure 3(d) displays the position of the front x_f as a function of time: the growth velocity of the dense state is not constant, and decreases from 500 to 250 nm/s.

Figures 3(b) and (c) show that concentration profiles in the dense state are almost stationary, with a clearly visible hump in the $x = 0$–$1\,\text{mm}$ range. Figures 3(b) and (c)

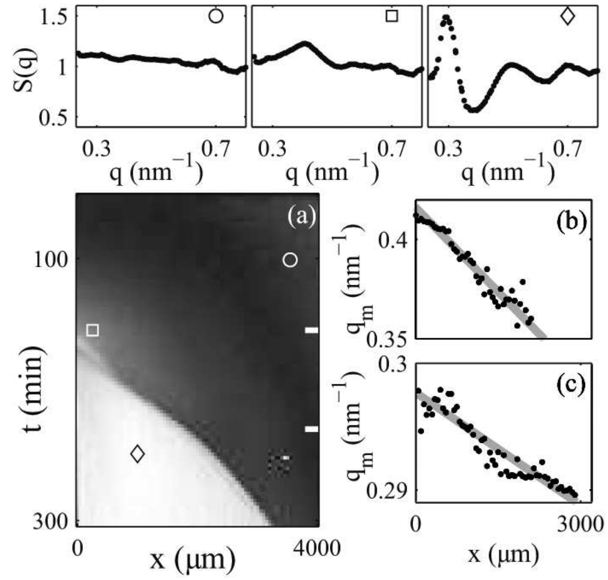

Fig. 4. Top: three typical measured $S(q)$ at the positions indicated by the symbols in (a). (a) Space-time plot of the standard deviation of $S(q)$. (b-c): positions of first peak against x at the times indicated by the white ticks on (a). Panel (b) corresponds to the liquid state at $t = 155\,\text{min}$, (c) to the solid one at $t = 230\,\text{min}$.

also show that for $t < 230\,\text{min}$, concentration fields in the dilute phase (before the front), are almost stationary, but that at larger time scales, the concentration profiles seem to *translate* in the x-direction, and the transition between the two states occurs between two fixed values ($\phi \approx 15$ to 30%, fig. 3(c)). For $t < 230\,\text{min}$, we can therefore assume that the incoming flux $j_0 = \phi_0 v_0$ is conserved up to the dense state. Its growth velocity v_f should therefore check the solute conservation, *i.e.*, $\phi_0 v_0 = \Delta\phi v_f$, where $\Delta\phi$ is the jump of solute concentration at the front. This is clearly demonstrated in fig. 3(d) where we estimate the front position x_f from the measurements of $\Delta\phi$ and the knowledge of $\phi_0 v_0$. The values of x_f significantly deviates from the measured one for $t > 230\,\text{min}$, as concentration profiles before the front are not stationary anymore.

3.3 Concentration process: structure factors measurements

We show in fig. 4 that the concentration process yields a hierarchy of structures as evidenced by the corresponding structure factors $S(q)$. For low concentrations ($\phi \leq 20\%$), $S(q)$ are almost constant. At intermediate ϕ ($> 20\%$), a shallow peak shows up at $\approx 0.38\,\text{nm}^{-1}$ indicating a slight degree of ordering between the charged NPs, and probably corresponding to the second order of the structure factor. Indeed, the maximal peak of $S(q)$ is expected to locate at $q < 0.2\,\text{nm}^{-1}$ for $\phi \leq 20\%$ (below our accessible q-range), if one assumes face-centered-cubic (fcc) arrangement. In the dense state, structure factors show now strong oscillations, with a first peak located at $\approx 0.29\,\text{nm}^{-1}$. Importantly, the transition observed on $S(q)$ upon concentration seems very abrupt, and does not simply correspond to a shift of the $S(q)$ first peak from the low q-range to the investigated q-window (see Movie F2 in the supplementary material).

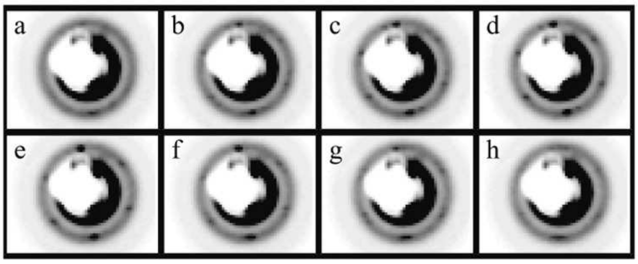

Fig. 5. SAXS patterns measured at positions $x = 400\,\mu\text{m}$ and at different times t, corresponding to different y-positions. The spatial resolution between two successive images is $0.5\,\mu\text{m}$. The patterns (b)-(g) shows well-defined azimuthal modulations, as compared to (a) and (h). These images thus indicate the presence of an organized *grain* of about $3\,\mu\text{m}$.

The spatio-temporal plot of fig. 4 represents the standard deviations of $S(q)$ coded using a gray level, and these data clearly demonstrate again a sharp transition between two differently organized states, that we now refer to as a *liquid* state, and a denser *solid* organized state. Importantly, the location of the peak position of $S(q)$ in the dense state leads to an estimate of the volume fraction in the 60–70% range according to a fcc arrangement, and thus far from the estimated $\phi = 30$–40% (see fig. 3). Again, we believe that our measurements of ϕ may present some uncertainties, and that our limited q-range does not allow us to extract properly the local concentrations from the $S(q)$ measurements. We thus hope to solve such a discrepancy by performing similar measurements at the *absolute scale*, and on a larger q-range.

Interestingly, the liquid and solid states undergo uniaxial compression. Indeed, while estimating the position q_m of the maximal peak of $S(q)$ (fig. 4(b), (c)), we observe that q_m slightly but significantly decreases both in the liquid state and in the solid one. This indicates a noticeable compressibility of these states which must be due to some flow of water still permeating across them and compressing them via a viscous drag.

3.4 Concentration process: 2D SAXS patterns

We now turn to the 2D SAXS patterns measured in the dense state. Some of these patterns show unexpected azimuthal modulations of the scattered intensity. More precisely, fig. 5 presents patterns measured at a given distance $x = 400\,\mu\text{m}$ from the tip of the channel but at different y-positions along the channel width. As the distance between two successive patterns is $0.5\,\mu\text{m}$, the size of the region explored here is about $3\,\mu\text{m}$ and the microfocused beam thus helps revealing the presence of *crystallytes* of typical size of 1 to $3\,\mu\text{m}$ in the dense state. We do not try here to assess the structure [21] of such small colloidal crystals, first because our q-range is too limited, but also because their finite sizes lead to a complex interpretation [22]. Moreover, as we are using a micro-focused X-ray beam (focal spot around $1.5 \times 1.5\,\mu\mathrm{m}^2$) crossing a channel of height $50\,\mu$m, we do not perform a perfect *averaged* measurement, as the probed scattering volume may only contains a few grains. This would also explain why structure factors $S(q)$ in such a dense state do not display thin and high peaks as measured on other ordered systems. The present results however unambiguously reveal that the NPs are locally ordered, on a micron grain size.

4 Discussions: towards quantitative measurements of collective diffusion coefficients

4.1 Theoretical description of the microevaporation process for the colloidal dispersion

Our experiments are similar to the classical sedimentation experiments of colloids leading to the growth of dense (and possibly crystallized) sediments. Importantly, microevaporation permits to concentrate NPs that would not sediment easily without strong centrifugation. Schindler and Ajdari [12] described the general case of microevaporation for binary mixtures, based on nonequilibrium, irreversible thermodynamics for which there is a coupling between pervaporation, hydrodynamics, and diffusion. They thus provided a general model to extract thermodynamic and kinetic information from the analysis of a microevaporation experiment, and more precisely from the combined measurements of the pervaporation-induced velocity profile $v(x)$ and the concentration field $\phi(x,t)$.

Importantly, our case is more complex than a simple binary mixture, since the charged dispersion contains more than two species: solvent, ions and colloids. Pervaporation thus also concentrates ions contained in the reservoir towards the microevaporator, and this can possibly change electrostatic interactions between the NPs during their concentration process.

However, as the effective charge carried by the Ludox NPs is around 50–70 [13,14] (a simple estimation using $4R/l_b$ [23] leads to 70, where l_b is the Bjerrum length), we can assume at a first approximation, that the ionic strength, and thus electrostatic interactions, is mainly dominated by the contribution of the counter-ions coming from the NPs only, as soon as the volume fraction is above 1%. In that case, the model developed by Schindler and Ajdari for binary mixtures is a good starting point to analyze our experiments.

In their model, the volume-averaged velocity profile $v(x)$ in the microevaporator follows,

$$\partial_x v(x) = -q(\phi), \tag{1}$$

where $q(\phi)$ reflects the loss of water via pervaporation, and thus depends on the chemical potential of water [12]. In the case of a dispersion, the colloidal assembly hardly affects the chemical potential of water, and thus also the evaporation rate. A rough estimation of the change in water chemical potential $\Delta\mu$ (the driving force of pervaporation) is indeed of the order of $\Delta\mu/kT = Z(\phi)v_m/v_c$, with $Z(\phi)$ the dispersion osmotic compressibility, and v_m/v_c the ratio of the volumes of water molecules over the colloid one. For our dispersion, $v_m/v_c \approx 3\cdot 10^{-6}$ and $\Delta\mu/kT$ is negligible. We can thus assume that $q(\phi) = \text{constant}$, and that the velocity profile is linear in the microevaporator, and given by

$$v(x) = -v_l - (v_0 - v_l)x/L_0, \tag{2}$$

with v_0 the incoming velocity and v_l a small *leakage* velocity coming from pervaporation in the PDMS matrix at the tip of the microevaporator. Calibration of our device leads to $v_0 = 5.5 \pm 0.5\,\mu$m/s and v_l in the 0.1–0.5 μm/s range (data not shown).

Solutes are transported in such a flow according to [12]

$$\partial_t\phi(x,t) = -\partial_x(\phi v(x) - D(\phi)\partial_x\phi), \tag{3}$$

where $D(\phi)$ is the long-time collective diffusion coefficient (also called *mutual* or *gradient* diffusion coefficient). $D(\phi)$ is intimately related to the colloidal interactions (osmotic compressibility), and also to the hydrodynamic interactions [24,25]. It thus differs from D_0, the self-diffusion coefficient of the NPs in the dilute regime.

4.2 Estimating collective diffusion coefficient

In the case of a linear velocity profile, and for a constant D, one can demonstrate from eq. (3) that solutes are convected from the reservoir up to an accumulation region of size $p \sim (DL_0/v_0)^{1/2}$ [9,11], coming from the competition between diffusion and convection by the pervaporation-induced flow. In that ideal case, the concentration rate in the accumulation zone is given by $\partial_t\phi = \phi_0 v_0/p$ [9,11]. Simple estimates of the extension of the spatial gradients p from the *bare* diffusion coefficient D_0 calculated from the Stokes-Einstein relation ($D_0 \approx 1.7\cdot 10^{-11}\,\mathrm{m}^2/\mathrm{s}$), give $p \approx 100\,\mu$m, and thus far from the observations. Indeed as shown in fig. 6, our experiments reveal that concentration profiles display smooth spatial gradients before the growth of the dense state, and the expected concentration rate $\partial_t\phi = \phi_0 v_0/p$ would also be too large to explain our results.

This points out that NPs interactions are crucial to understand the concentration process (spatial gradients and rates of concentration) that we observed for that charged suspension. Such interactions have to be taken into account in the collective diffusion coefficient $D(\phi)$.

Equation (3) reveals that it is possible to extract $D(\phi)$ from the measurements of the concentration field $\phi(x,t)$. Indeed, by estimating numerically the quantities $\partial_t\Psi(x,t) = \int_0^x \phi(u,t)\mathrm{d}u$ and $\partial_x\phi(x,t)$ from our measurements, we can estimate $D(\phi)$ for several concentrations by assuming that the velocity profile $v(x)$ is given by

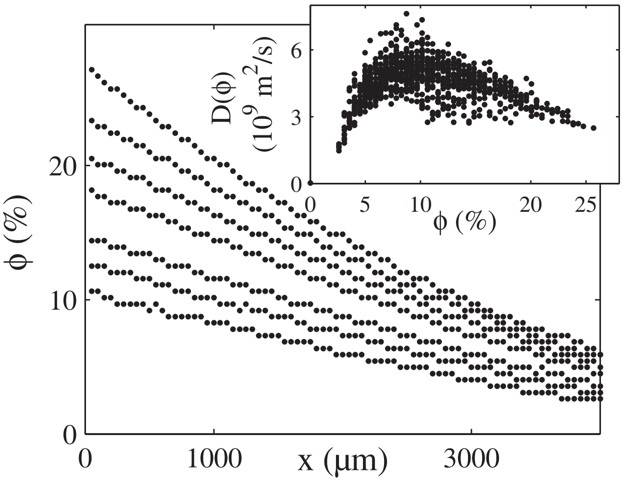

Fig. 6. Concentration profiles $\phi(x,t)$ before the growth of the dense state, in the range of time $t = 49$–141 min. Inset: estimate of the collective diffusivity $D(\phi)$ *vs.* volume fraction ϕ (see text).

eq. (2), and assuming a vanishing flux $\phi v(x) - D(\phi)\partial_x\phi$ at $x = 0$. We restrict such an analysis in the liquid state (for $\phi < 25\%$) as our measurements are not resolved enough to yield precise values of the spatial derivatives in the dense state.

The results obtained by such a procedure are shown in the inset of fig. 6. The numerical derivatives of the data lead to a significant noise in such calculations, but one can see a clear behavior. First, the values of $D(\phi)$ are larger than the value of the Stokes-Einstein diffusivity ($D(\phi) \approx 5 \cdot 10^{-9}\,\mathrm{m}^2/\mathrm{s}$ *vs.* $D_0 \approx 1.7 \cdot 10^{-11}\,\mathrm{m}^2/\mathrm{s}$), as it is the case for repelling NPs (the relaxation of the gradients of concentration are mainly due to the strong electrostatic interactions). Secondly, $D(\phi)$ increases up to reach a maximum around $\phi \approx 10\%$, and seems to decrease again at higher volume fractions. This general behavior of charged suspensions is due to the interplay between osmotic compressibility of the dispersion and hydrodynamic interactions. At low volume fraction, $D(\phi)$ increases as the osmotic compressibility decreases with increasing concentrations. Above a critical concentration, hydrodynamic hindrance compensates the electrostatic repulsions, and $D(\phi)$ decreases with increasing ϕ [24–26].

Such observations also recall the extended sedimentation profiles for charged colloids [27,28], and more recently in consolidation experiments [29]. For the case of sedimentation, a one-component description is sufficient to explain the observed sedimentation profiles [30]. A fully detailed description of the concentration process of all the ionic species (NPs and ions), taking into account the finite diffusivity of the ions, and all the interactions (hydrodynamic and electrostatic), is missing in the context of evaporation, and left for a future work. Interestingly, precise measurements of $S(q)$ and $\phi(x,t)$ in our experiments may give new insights in the understanding of the dynamics of charged suspensions upon consolidation. Indeed, simultanenous measurements of $S(q)$ in a larger q-range will lead to an estimate of the osmotic compressibility, and therefore should provide *direct* information on the hydrodynamic interactions.

5 Conclusions and outlooks

As for the case of sedimentation of colloids, we observe upon concentration the nucleation and growth of a dense organized phase, but at a relatively low concentration $\phi \approx 30\%$ compared to the case of hard spheres ($\phi_c \approx 50\%$), due to the repulsive electrostatic interactions [24]. Furthermore, our SAXS microfocused resolution permits to evidence crystalline grains inside this dense state with small sizes (1–3 μm) that may have not been identified previously in SAXS investigations of phase diagrams of charged colloids [31]. Repulsive *ionic* colloidal crystals are often observed in phase diagrams of highly deionised suspensions of large colloids (> 100 nm in diameter), and at low volume fractions. They have however been rarely reported in more concentrated systems ($\phi > 10\%$) with smaller elementary building blocks (< 20 nm in diameter), except in a few pieces of work as in ref. [32] in a rather similar system (charged silica NPs, radius 10 nm). As noted in this work [32], nucleation and growth of such crystals, as well as their structure, is still poorly understood and may probably differ from the case of highly deionised suspensions of larger colloids. The typical lattice dimension (≈ 50 nm) in such cases may also lead to *photonic* applications but for a smaller wavelength compared to the classical Bragg reflections observed in the visible range with larger colloids.

We also expect to be able to enhance the crystallinity of the dense state by tuning both the concentration rate, as for the case of sedimentation, and the interaction between particles. In such a way, we hope to build well-defined lattices of functional NPs, that are believed to be good candidates of metamaterials working in the visible range. Finally, it is well known that tuning interactions between NPs is the best method to promote nanoscale self-assembly [33]. However, transport properties (such as the collective diffusion coefficient) are also crucial to help and understand the self-assembly process, especially during evaporation of the solvent of a dispersion [3]. We believe that microevaporator tools, coupled with analytical methods such as microfocused SAXS, may prove to be useful to bring such information.

This work has been done within LTP SC2267 at ESRF. We acknowledge the important participation of M. Burghammer, R. Davies, and F. Nallet for fruitful discussions. We thank Région Aquitaine, Université Bordeaux-1, Rhodia, and CNRS for funding and support. The research leading to these results has also received funding from the European Union's Seventh Framework Programme (FP7/2008) under grant agreement n°228762 and from Agence Nationale de la Recherche for grant DNATOOL n°07-NANO-001 in the PNANO framework.

References

1. E.V. Shevchenko, D.V. Talapin, N.A. Kotov, S. O'Brien, C.B. Murray, Nature **439**, 55 (2006).
2. J.A. Fan, C. Wu, K. Bao, J. Bao, R. Bardhan, N.J. Halas, V.N. Manoharan, P. Nordlander, G. Shvets, F. Capasso, Science **328**, 1135 (2010).
3. P. Podsiadlo, G. Krylova, A. Demortière, E.V. Shevchenko, J. Nanopart. Res. **13**, 15 (2011).
4. T.P. Bigioni, X.M. Lin, T.T. Nguyen, E.I. Corwin, T.A. Witten, H.M. Jaeger, Nat. Mater. **5**, 265 (2006).
5. S. Narayanan, J. Wang, X.M. Lin, Phys. Rev. Lett. **93**, 135503 (2004).
6. S.V. Roth, T. Autenrieth, G. Grübel, C. Riekel, M. Burghammer, R. Hengstler, L. Schulz, P. Müller-Buschbaum, Appl. Phys. Lett. **91**, 091915 (2007).
7. R.D. Deegan, M. Balkanski, T.F. Dupont, G. Huber, S.R. Nagel, T. Witten, Nature **389**, 827 (1997).
8. T.A. Witten, Europhys. Lett. **86**, 64002 (2009).
9. J. Leng, B. Lonetti, P. Tabeling, M. Joanicot, A. Ajdari, Phys. Rev. Lett. **96**, 084503 (2006).
10. J. Leng, M. Joanicot, A. Ajdari, Langmuir **23**, 2315 (2007).
11. J.B. Salmon, J. Leng, J. Appl. Phys. **107**, 084905 (2010).
12. M. Schindler, A. Ajdari, Eur. Phys. J. E **28**, 27 (2009).
13. H. Ning, J.K. Dhont, S. Wiegand, Langmuir **24**, 2426 (2008).
14. G.H. Bolt, J. Phys. Chem. **61**, 1166 (1957).
15. R. Barrett, M. Faucon, J. Lopez, G. Cristobal, F. Destremaut, A. Dodge, P. Guillot, P. Laval, C. Masselon, J.B. Salmon, Lab Chip **6**, 494 (2006).
16. R. Dootz, H. Evans, S. Köster, T. Pfohl, Small **3**, 96 (2007).
17. L. Pollack, M.W. Tate, A.C. Finnefrock, C. Kalidas, S. Trotter, N.C. Darnton, L. Lurio, R.H. Austin, C.A. Batt, S.M. Gruner *et al.*, Phys. Rev. Lett. **86**, 4962 (2001).
18. ID13, European Synchrotron Radiation Facility, Grenoble, France; $\lambda = 0.994\,\text{Å}$, focal spot $1.5 \times 1.5\,\mu\text{m}^2$.
19. R. Davies, M. Burghammer, C. Riekel, Synchr. Radiat. Nat. Sci. **5**, 96 (2006).
20. P. Lindner, T. Zemb (Editors), *Neutron, X-rays & Light: Scattering Methods Applied to Soft Condensed Matter* (North-Holland Delta Series, 2002).
21. S. Hu, Y. Men, S.V. Roth, R. Gehrke, J. Rieger, Langmuir **24**, 1617 (2008).
22. S. Förster, A. Timmann, C. Schellbach, A. Fromsdorf, A. Kornowski, H. Weller, S.V. Roth, P. Lindner, Nat. Mater. **6**, 888 (2007).
23. L. Belloni, Colloids Surf. A: Physicochem. Eng. Aspects **140**, 227 (1998).
24. W.B. Russel, D.A. Saville, W.R. Schowalter, *Colloidal Dispersions* (Cambridge University Press, 1989).
25. G. Nagële, Phys. Rep. **272**, 215 (1996).
26. M. Drifford, L. Belloni, J. Dalbiez, A.K. Chattopadhyay, J. Colloid Interface Sci. **105**, 587 (1985).
27. R. Piazza, T. Bellini, V. Gegiorgio, Phys. Rev. Lett. **71**, 4267 (1993).
28. M. Rasa, A.P. Philipse, Nature **429**, 857 (2004).
29. A. Sarkar, M.S. Tirumkudulu, Langmuir **25**, 4945 (2009).
30. L. Belloni, J. Chem. Phys. **123**, 204705 (2005).
31. E.B. Sirota, H.D. Ou-Yang, S.K. Sinha, P.M. Chaikin, J.D. Axe, Y. Fujii, Phys. Rev. Lett. **62**, 1524 (1989).
32. J. Chang, P. Lesieur, M. Delsanti, L. Belloni, C. Bonnet-Gonnet, B. Cabane, J. Phys. Chem. **99**, 15993 (1995).
33. K.J.M. Bishop, C.E. Wilmer, S. Soh, B.A. Grzybowski, Small **5**, 1600 (2009).